ADVANCED FUNCTIONAL MATERIALS
www.afm-journal.de

Tailored Silica Macrocellular Foams: Combining Limited Coalescence-Based Pickering Emulsion and Sol–Gel Process

Mathieu Destribats, Benjamin Faure, Marc Birot, Odile Babot, Véronique Schmitt, and Rénal Backov**

Solid-sate monolithic macrocellular foams are synthesized by mineralizing the continuous phase of oil-in-water Pickering emulsions, used as templates, with the sol–gel process. For the first time, taking advantage of the limited coalescence phenomenon occurring in emulsions stabilized by solid particles, concentrated emulsions with calibrated drop size are produced, leading to the synthesis of monolithic foams with nearly monodisperse macroscopic voids. Such a strategy allows independent tuning of the macrocellular void diameters from 20 to 800 μm and the diameter of the windows connecting adjacent cells. The obtained macrocellular foams also bear micro- and mesoporosity, leading to Brunauer, Emmet and Teller (BET) surface area values between 700 and 900 $m^2 g^{-1}$ with a good mesopores monodispersity.

1. Introduction

Rational design of porous monolith materials is nowadays a highly competitive field of research due to the wide scope of associated applications in separation techniques, absorbers, heterogeneous catalysis, optics, acoustic and thermal insulators, and so forth.[1–6] In this context of generating complex architectures through a strong rational design, the concept of integrative chemistry[6–9] has emerged from the interface between bio-inspired approaches,[10–12] general soft chemistry, including hybrid organic–inorganic chemistry,[13–15] and the physical chemistry of complex fluids. Current synthetic paths to build organized inorganic materials include, for instance, coupling of multiplex templating processes combining self-assembled surfactants with larger moulds as emulsion droplets,[16,17] air–liquid foams,[18–25] latex beads,[26,27] or by applying external stimuli.[28–30] One way of generating such architectures is to use either direct concentrated aqueous[31] or non aqueous emulsions[32] as macroscopic templates. On the basis of Imhof and Pine's[16,31] work, we reported on the way of elaborating macrocellular silica monoliths[17] that we labeled Si(HIPE), in reference to the first generation of porous organic polymers obtained through the use of concentrated reverse emulsions, known under the polyHIPE acronym that stands for polymerized high internal phase emulsion.[33–35] Also it is important to notice that HIPEs coming either from the polymer or sol–gel communities can be nicely hybridized to promote advanced functional materials bearing enhanced and versatile properties.[36–49]

Herein, we propose a method to realize good control over the final macroscopic cell sizes and morphologies by tuning both the initial drops size and the oil volume fraction of the initial emulsion. An easy way to achieve such control consists in replacing the usual surfactants by colloidal particles adsorbed at the oil–water interface. Such emulsions are known as Pickering emulsions and, depending on the nature of both particles and oils, it is possible to formulate either oil-in-water (called direct emulsions) or water-in-oil emulsions (also called reverse emulsions).[50–52] For instance, Bon and Colver[53] prepared cellular monoliths of poly(divinylbenzene) using Pickering water-in-oil emulsions stabilized by latex nanoparticles, and Bismarck et al.[54] generated monoliths from water-in-oil Pickering emulsions using silica nanoparticles modified with oleic acid. In addition, carbon nanotubes can be used to stabilize water-in-oil Pickering emulsion to formulate polyHIPE.[55,56] The generation of macroporous scaffolds originating from oil-in-water Pickering emulsions has been more seldom reported than have water-in-oil ones. However, several macrocellular ceramics (alumina, silica, iron oxide) have been obtained using oil-in-water Pickering emulsions.[57,58] It has been shown that stabilization with particles hinders extensive droplet coalescence during solvent extraction, allowing drying and sintering of the emulsions directly into macroporous materials in the absence of any chemical reaction. In the same way, silica foams have been obtained where final silica dense ceramics are generated simply through volatile oil (or toluene) and water evaporation.[59]

Particle-stabilized emulsion templating provides undoubtedly a facile methodology to generate porous materials; formulations of starting emulsions bearing a good monodispersity can be advantageously achieved by taking advantage of the limited

Dr. M. Destribats, B. Faure, Dr. V. Schmitt,
Prof. R. Backov
Université de Bordeaux
C.R.P.P. U.P.R. C.N.R.S. 8641
115 Avenue Albert Schweitzer, 33600 Pessac, France
E-mail: schmitt@crpp-bordeaux.cnrs.fr;
backov@crpp-bordeaux.cnrs.fr
Dr. M. Birot, O. Babot
Université de Bordeaux
I.S.M. U.M.R. C.N.R.S. 5255
351 Cours de la Libération, 33405 Talence, France

DOI: 10.1002/adfm.201102564

coalescence phenomenon[52,60,61] occurring in Pickering emulsions We have recently generated nearly monodisperse thermoresponsive capsules (wax@SiO_2 core–shell particles) with a controlled size exploiting the above-mentioned limited coalescence phenomenon.[62] In this work we make use of nearly monodisperse Pickering emulsions as templates to generate silica macrocellular foams bearing macroscopic pores with tailored sizes (from a few microns to 1 mm) and very narrow size distributions. These foams series are labeled Si(PHIPE), for silica Pickering-based high internal phase emulsion.

2. Experimental Section

2.1. Materials

Hexadecane of high purity (greater 99%) and polydimethylsiloxane (100 mPa S; PDMS) were purchased from Aldrich. The monomer tetraethylorthosilicate (TEOS) and the surfactant cetyltrimethylammonium bromide (CTAB) were purchased from Sigma-Aldrich and Fluka, respectively. Aerosil silica nanoparticles R816 (diameter 12 nm) were provided by Degussa Evonik. Hydrochloric acid (HCl) 37% was purchased from Prolabo. All the chemicals were used as received without further purification.

2.2. Syntheses

2.2.1. Particle Modification

Aerosil R816 are silica nanoparticles hydrophobized by chemical grafting of hexadecylsilane that confers them an amphiphilic behavior: the particles are partially wetted by both oil and water phases and therefore adsorb at the oil–water interface. Even when used as received, these particles were able to stabilize oil-in-water emulsions, however control over the mean drop size of emulsions was rather difficult. Better control was obtained after further surface modification of the particles by adsorbing a very low amount of a cationic surfactant, namely cetyltrimethylammonium bromide (CTAB). In the following experiments, silica particles were systematically modified prior to use: aerosil particles were first dispersed into distilled water, then cationic surfactant molecules were introduced in order to electrostatically adsorb at the negatively charged silica surface, as already described elsewhere.[61] Following the same protocol, the amount of surfactant was adapted to the total mass of particles in order to maintain the same specific coverage of 13 nm^2 of silica surface per CTAB molecule at the silica/water interface. This value was estimated with the assumption that all the surfactant from the bulk was consumed to cover the silica surface. Despite of the use of small amount of CTAB, the emulsions are not stabilized by the surfactant but by the functionalized particles, as can be deduced from the obtained large drop sized monodisperse emulsions.

2.2.2. Emulsion Formulation

Typical aqueous phases were prepared by adding to the particles dispersions, at various concentrations, the same volume (as the dispersion) of HCl (37%) and the same volume of TEOS under magnetic stirring. As a direct consequence, the obtained solution is therefore composed of equal volumes of the particles dispersion, HCl solution and TEOS solution, each of them corresponding to a third of the total volume. The as-formulated aqueous phases were left under stirring for few minutes in order to perform TEOS hydrolysis to generate silicic acid $Si(OH)_4$, leading to a decrease and disappearance of the aqueous phase turbidity. Then, the oily phase (hexadecane or PDMS) was directly added at once before emulsification. The oil phase volume fraction was varied from 64% to 90%. Emulsification was performed by means of an Ultra-Turrax homogenizer (T25 Janke & Kunkel) equipped with a S25 KV-25F rotor head operating at 24 000 rpm for 1 min for hexadecane and at 9500 rpm for 1 min when PDMS was used (a too strong turbulent flow resulted in uncompleted oil incorporation for the viscous PDMS). In this article, the emulsions are labeled $_X$(PHIPE)$_{YZ}$ where X is the amount of particles used to stabilized the emulsion with respect of the total oil weight (mg g^{-1}), Y is the oil volume fraction (%) with respect to total sample volume, and Z the nature of the oil phase (H for hexadecane, P for PDMS). It is worth noting that emulsions prepared at pH 7 are identical to the ones prepared with concentrated HCl concentration meaning that pH does not modify the CTAB adorption on the silica nanoparticles.

2.2.3. Silica Macrocellular Foam Si(PHIPE) Synthesis

In such acidic conditions, mineralization of the aqueous phase occurred very quickly but emulsions were left at rest for a 10 days period in order to fully complete the sol–gel process. In a second step, the monoliths were washed by immersion in a tetrahydrofuran/acetone (7:3 v/v) mixture three times over a 24 h period in order to remove the aqueous and oily phases, and then they were dried slowly by air in a dessicator for one week. As a result, the materials are highly interconnected porous monoliths labeled $_X$Si(PHIPE)$_{YZ}$. Finally, to remove any remaining organic traces and to mechanically strengthen by sintering the silica macrocellular foams, the materials were thermally treated as follows: the first step consisted of a heating ramp at 2 °C min^{-1} to 200 °C. Then, this temperature was hold for 2 h before a second ramp at 2 °C min^{-1} was imposed to reach 650 °C. This temperature was held for 6 h. The cooling process was uncontrolled and directed by the oven inertia. Final macroporous foams are made exclusively of silica.

2.3. Characterization

Optical microscopy characterization was performed using an inverted optical microscope Zeiss Axiovert X100. The emulsion size distribution was estimated by image analysis: the dimensions of about 50 droplets were measured so that both the surface average diameter D and the polydispersity P could be estimated:

$$D = \frac{\sum_i N_i D_i^3}{\sum_i N_i D_i^2} \text{ and } P = \frac{1}{\bar{D}} \frac{\sum_i N_i D_i^3 \left| \bar{D} - D_i \right|}{\sum_i N_i D_i^3}$$

where N_i is the total number of droplets with diameter D_i. $\overline{D}$ is the median diameter, i.e., the diameter for which the cumulative undersized volume fraction is equal to 50%. In the following, emulsions characterized by a P value lower than 20% will be considered as monodisperse. Emulsions obtained from limited coalesence process exhibit narrow size distributions, in such conditions 50 droplets are truly representative of the emulsion

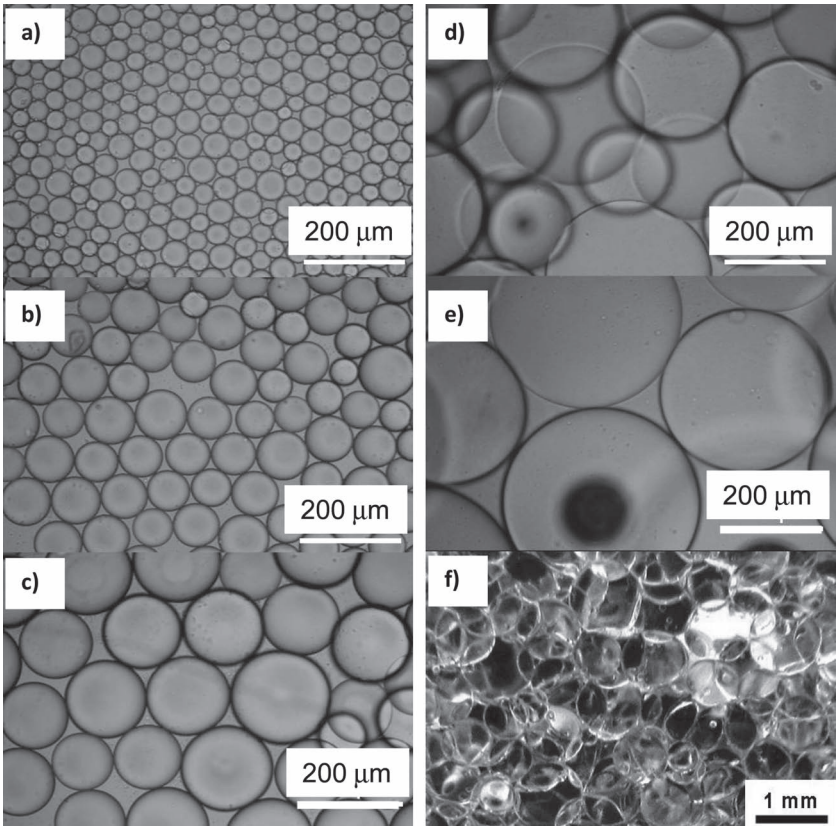

Figure 1. Optical microscopic images of controlled-size emulsions: a) $_{11.4}$(PHIPE)$_{64H}$, b) $_{4.8}$(PHIPE)$_{64H}$, c) $_{2.6}$(PHIPE)$_{64H}$ d) $_{5.5}$(PHIPE)$_{64P}$, and e) $_{3.7}$(PHIPE)$_{64P}$. f) $_{1.1}$(PHIPE)$_{64P}$ macroscopic picture of a PDMS-in-water emulsion composed of millimetric drops.

drop size. Scanning electron microscopy (SEM) observations were performed with HITACHI TM-1000 apparatus at 15 kV. Surface-area and pore characteristics on the mesoscale were obtained using a Micromeritics ASAP 2010 apparatus. Intrusion/extrusion mercury measurements were performed using a Micromeritics Autopore IV 9500 porosimeter. Transmission electron microscopy (TEM) observations were performed with a HITACHI-H600 microscope operating at 75 KV. The foams were crashed into powder, dispersed in ethanol, spread over carbon coated-gold TEM grids and finally left to dry in air.

3. Results and Discussion

3.1. Starting Emulsions

Limited coalescence[61] consists of producing a large excess of oil–water interface compared with the interfacial area that can be covered by the solid particles. Hence, for this process to occur, the systems must be formulated in the presence of a very small amount of solid particles. When the mechanical agitation is stopped, the partially unprotected droplets coalesce, thus reducing the total amount of oil–water interface. Since the particles are irreversibly adsorbed, the coalescence process stops as soon as the oil–water interface is sufficiently covered. The resulting emulsions are characterized by narrow size distributions and are stable over months. Moreover, since the evolution of the droplets inverse mean diameter versus the particle-to-oil weight ratio is linear, the size can be controlled by adjusting the amount of particles.[61–63] Exploiting this phenomenon we produced monodisperse oil-in-water emulsions over a wide range of droplet diameters, from the micrometer to the millimeter, as illustrated by **Figure 1**. As expected, a decrease of the amount of silica nanoparticles stabilizer promotes an increase of the droplet diameter.

As can be seen from **Figure 2**, limited coalescence occurs, whatever the chosen oil (hexadecane or PDMS). One can notice that, with the same amount of particles, hexadecane drops are smaller than PDMS ones, revealing a difference in particle adsorption at the oil–water interface. From the slopes of the curves in Figure 2 and using simple geometrical considerations (see the Supporting Information for details), one can estimate an average number of silica layers surrounding the oil drops. For hexadecane and PDMS in water emulsions, drops are covered by 4 and 15 layers of particles on average, respectively. These difference likely results from the two different stirring speeds input during emulsification. Indeed silica particles are initially aggregated in the aqueous phase so that clusters of particles adsorb at the interface during emulsification. It is hence not surprising that the size of the particle clusters (and then the estimated average number of layers) depends upon the agitation energy.

3.2. Limited Coalescence-Based Solid foams

The strategy of using Pickering emulsions offers a double advantage. Firstly, as explained above, it promotes narrow droplets size distributions and drop size control owing to limited coalescence. Secondly, the silica nanoparticles adsorbed at the oil–water interface will serve as nucleation sites when the sol–gel process occurs within the hydrophilic continuous phase. In crystal growth, one distinguishes two nucleation types, namely homogeneous and heterogeneous ones. Homogeneous nucleation occurs within the bulk solution and new interfaces between the growing nuclei and the solution are being created, requiring thereby an additional surface energy. Heterogeneous nucleation occurs on pre-existing nuclei or interfaces where energy associated to the creation of a new solid/liquid interface is minimized. Therefore, heterogeneous nucleation is promoted on the pre-existing silica particles adsorbed at the interface. Once initiated from the interface, the sol–gel network extends easily throughout the low volume of continuous phase because of the silica precursor high concentration.

In a first set of experiments, we chose to fix the dispersed phase volume fraction at 64% and to vary the initial drop sizes (by varying the amount of particles). The resulting templated

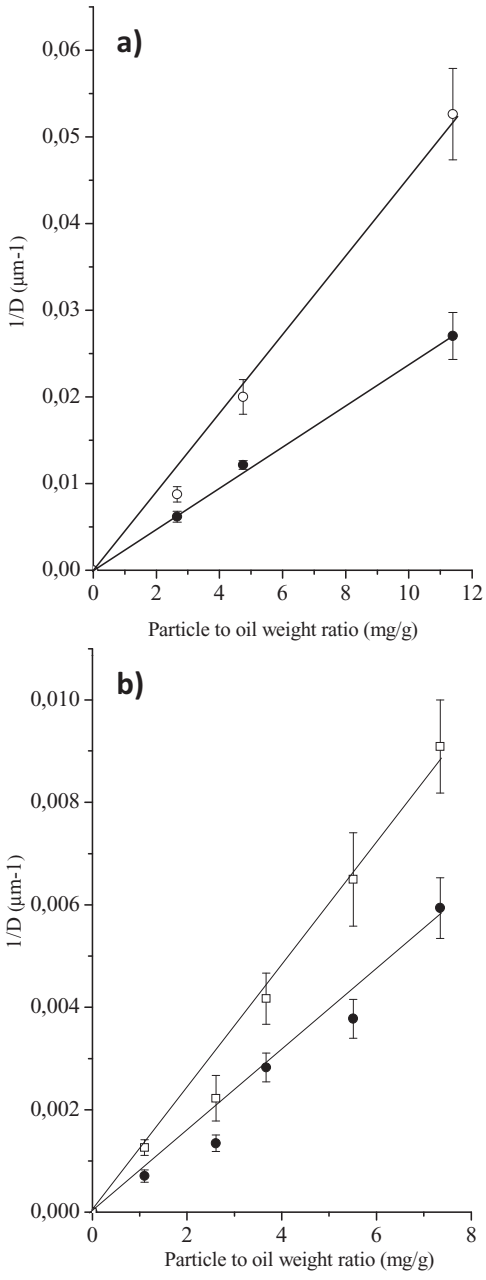

Figure 2. Evolution of the inverse mean diameter ($1/D$) of starting emulsion drops (●) and generated pores through condensation and drying (□) as a function of the particle-to-oil weight ratio: a) hexadecane and b) PDMS. The oil volume fraction of the initial emulsions is 64%.

materials are self-standing monoliths (**Figure 3**), characterized by macropores resulting from the initial drops. SEM pictures shown in **Figure 4** show the foams obtained after mineralization and drying of the emulsions reported in Figures 1 and 2, when the sol–gel process is finished. As for the emulsion drop size, the obtained foams macropores are monodisperse (P values lower than 20%). Their inverse mean diameters are also reported in Figure 2. Whatever the emulsion oil phase, the macropores are smaller than initial emulsion drops, showing that shrinkage occurred during solidification and

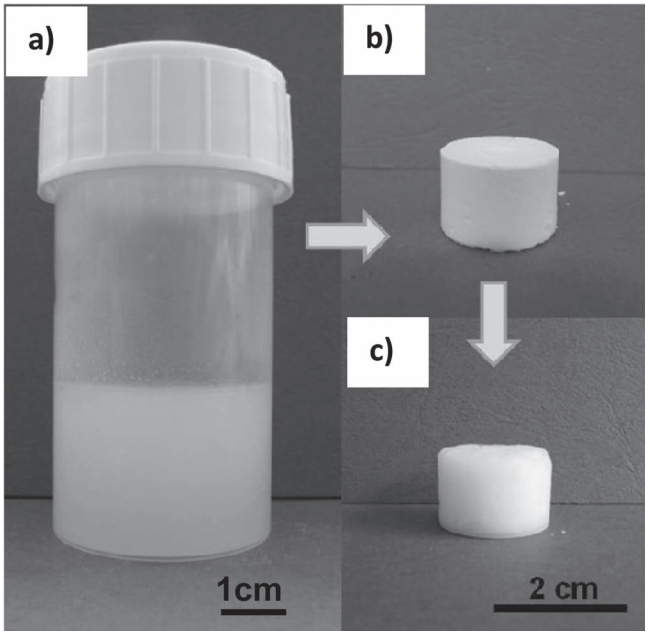

Figure 3. Example of the volume evolution through the monolith synthesis: a) mineralized HIPE, b) porous monolith material after washing and drying, and c) porous monolith material after sintering by thermal treatment. Panels (b,c) have the same scale bar.

mainly during drying, owing to capillary forces. This high shrinkage promoted through drying is indeed related to the acidic conditions of polycondensation. We have to keep in mind that the pH at which mineralization is driven is rather acidic since $[H_3O^+] \approx 4$–6 M; this is to say lower than the silica isoeletric point reached at pH around 2.1. This means that the growing inorganic polymer is sufficiently dense (Euclidian) to offer good mechanical strength (dense walls) in balance with a fractal character that allows the inorganic growing network to accommodate the oil droplets curvature. The first consequence of the sol fractal character addressed without charged mesophases is that the shrinkage during the drying process will be enhanced as capillary forces will further compact the inorganic scaffold. Comparing the slopes in Figure 2 representing the emulsion drops and the foam pores sizes, it is found that the drop/macropore diameters ratios are equal to 2.26 and 1.70 for hexadecane and PDMS, respectively. This corresponds to the volumes contracting, after mineralization and drying, by factors of 11.5 and 4.9, respectively. The contraction factor (estimated from the cube of the drop macropore) detected at a micrometer scale can be compared with the macroscopic volume evolution at each step of the foam synthesis (Figure 3).

Macroscopically, mineralization itself does almost not modify the volume that first decreases during the next drying step by factors of 8.5 and 3.3 for hexadecane and PDMS, respectively (estimated from the monolith dimensions). Although very close, the microscopic and macroscopic shrinkage rates are somewhat different. The observation of this difference means that walls, which are not taken into account in the estimation based on the drop-macropore diameter comparison, also contract with a smaller effect. On the contrary, estimations based on the

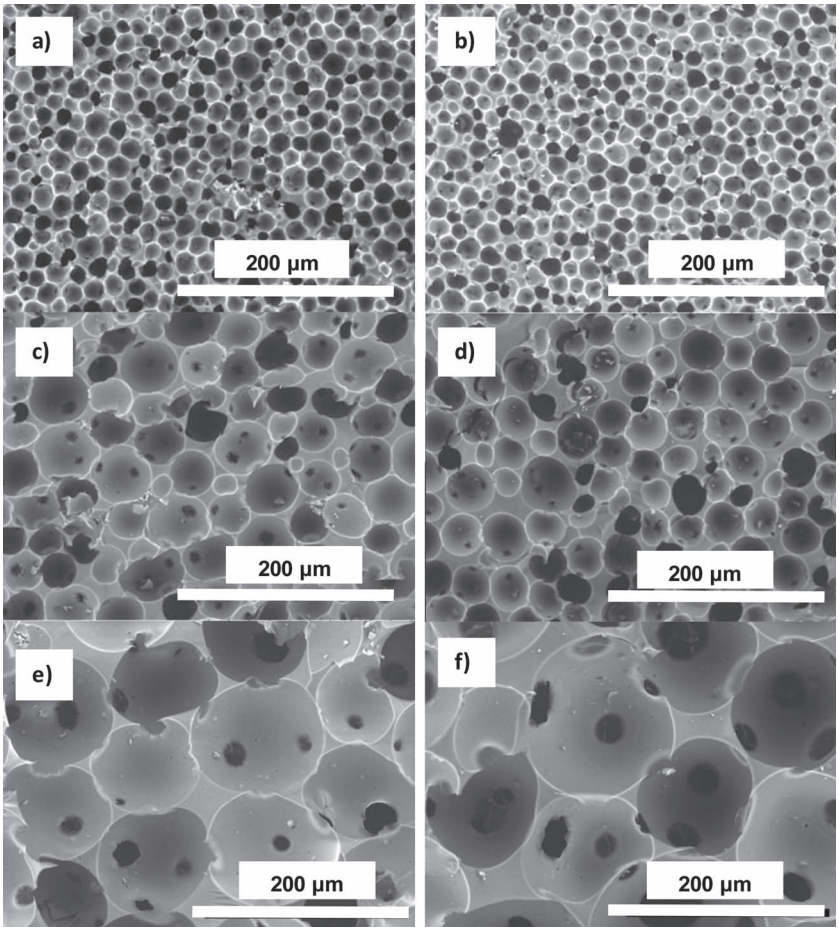

Figure 4. SEM images of solid foams synthesized from 64 vol-% of hexadecane-in-water emulsions varying the amount of particles: a,b) $_{11.4}$Si(PHIPE)$_{64H}$, c,d) $_{4.8}$Si(PHIPE)$_{64H}$, and e,f) $_{2.6}$Si(PHIPE)$_{64H}$. Materials are observed either after drying (a,c,e) or after thermal treatment (b,d,f).

macroscopic volumes take into account the whole material and are therefore a mean value of both voids large shrinkage and smaller walls sintering. Next, thermal treatment produces a further contraction to reach a total volume decrease by factors of 10.6 and 4.3, respectively. Note that sintering is isotropic (estimated from the monolith dimensions after thermal treatment). Shrinkage is much less pronounced for material based on PDMS as dispersed phase, probably because the larger number of silica layers favors resistance against contraction due to capillarity during drying, the silica particles bearing intrinsically a strong Euclidian (dense) character. This means that through choice of mixing speeds during emulsification one can control the way particles adsorb and therefore tune the rigidity that governs material contraction. The second consequence of both the heterogeneous nucleation starting at the oil/water interface and the inherent dual fractal/Euclidian character of the growing inorganic network, is that the full volume of the continuous hydrophilic phase is mineralized (Figure 4). If conventional charged surfactants are used to stabilize the oil/water interface of emulsions, only the oil/water interface regions are mineralized where the macroscopic morphology resembles to aggregated hollow spheres.[17] As shown in Figure 4, we notice that the oil droplet monodispersity is neither altered through the mineralization process, nor during the thermal treatment applied to sinter the porous ceramic. Besides the monodispersity of the macropores, Figure 2 shows that their size is well controlled despite sintering because the associated shrinkage is homothetic. Another important issue is that the macroscopic pores are connected so that the porosity is said open; this feature is particularly obvious in Figure 4c–f.

The same trends are observed (**Figure 5**) when PDMS is used as the oily phase: monodisperse macropores, open macroporosity, and full mineralization of the continuous hydrophilic phase. The only difference lies in the larger size of the macropores, in total agreement with both the larger emulsion drops size and the smaller shrinkage factor, as discussed previously.

In summary, we can generate Si(PHIPE) monoliths characterized by a good monodisperse character of the macroscopic void space diameters ranging from 20 to 160 µm for the $_{X}$Si(PHIPE)$_{64H}$ series while the range of void diameters is 105 to 800 µm for the $_{X}$Si(PHIPE)$_{64P}$ series. At such high sizes, the macropores are visible by the naked eye (**Figure 6**).

Beyond SEM investigations it is important, to better characterize these new materials, to provide more quantitative data concerning both foams macroscopic pore dimensions and skeleton characteristics. We thus performed mercury porosimetry experiments to reach foam-specific signatures toward percentage porosity and intrusion volume, as well as bulk and skeleton densities; these data are given in **Table 1**.

As observed within Table 1, the intrusion volume is mainly increasing with the amount of silica nanoparticles used to stabilize the emulsion diminishes. Also, when considering the two kind of oils in use, for the same amount of silica nanoparticles employed to stabilize the starting emulsions the percentage porosity of the $_{X}$Si(PHIPE)$_{64P}$ series is higher than that of the $_{X}$Si(PHIPE)$_{64H}$ one. Despite the same initial drop volume fraction of 64%, PDMS-based monoliths are more porous than their hexadecane-based homologous. On one hand, we have to remember that hexadecane drops are covered by fewer particles (4.3 layers vs. 14.8 for PDMS drops) and that they shrink more (2.26 vs. 1.7 for PDMS during mineralization and drying), leading to a higher volume contraction rate (11.5 vs. 4.9 for PDMS). Such a high contraction (two times larger than for the $_{X}$Si(PHIPE)$_{64P}$ foam series) favors rupture of the films during mineralization and thereby increases the diameter of the connecting windows, but decreases the overall porosity. On the other hand, considering the wide range of drop size (from microns to millimeter), we cannot disregard creaming phenomenon (because of the density mismatch between oil and water) that is susceptible to occur before the freezing of the material structure at mineralization completion. It is likely that, in the case of big drops, buoyancy produces a more concentrated cream

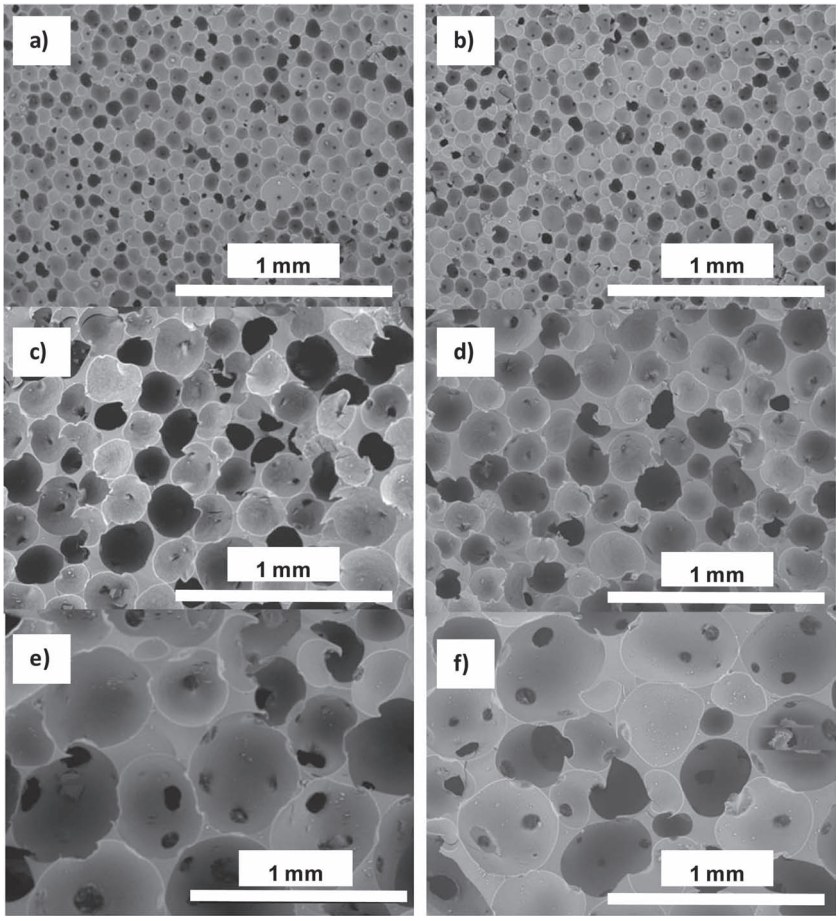

Figure 5. SEM images of solid foams synthesized from 64% PDMS-in-water emulsions: a,b) $_{7.3}$Si(PHIPE)$_{64P}$, c,d) $_{3.7}$Si(PHIPE)$_{64P}$, and e,f) $_{2.5}$Si(PHIPE)$_{64P}$. Materials are observed either after drying (a,c,e) or after thermal treatment (b,d,f).

than the usual random close packing of emulsions (64 vol-%). This effect is quicker as the drop size increases and could occur faster than the locked-evolution of the material architecture induced by mineralization. This phenomenon could be the origin of the porosity higher than 64% observed for the PDMS series and at the origin of the increasing porosity measured for the hexadecane series as the drop diameter increases (as the amount of silica nanoparticles used to stabilize the emulsion diminishes). As a direct consequence of these two combined effects, similar foam morphologies can be obtained with two initially different emulsions, $_{2.6}$Si(PHIPE)$_{64H}$ and $_{7.3}$Si(PHIPE)$_{64P}$; one can say that minimizing the oil/water interface with 2.6 mg of silica nanoparticles per gram of hexadecane provides, finally, approximately the same solid-state foam as that obtained with PDMS at 7.3 mg of silica nanoparticles per gram of oil.

So far we have kept the oil volume fraction constant, varying only the amount of stabilizing silica nanoparticles. This strategy allowed control over the drop size and consequently the pore size. Elaboration of macrocellular foams by templating Pickering emulsions obtained by exploiting limited coalescence also allows control over the foam macroporosity and consequently the windows connecting adjacent cells, keeping the macropore size constant. To trigger this issue we did maintain the silica nanoparticle-to-oil weight ratio constant (in order to keep a constant drop diameter) while varying the oil volume fraction. As observed in **Figure 7**, when the oil volume fraction increases, the resulting macroscopic pore diameters remain quasi-constant around 160 µm but the size of the windows connecting adjacent cells increases.

As mentioned above, it is important to perform mercury porosimetry experiments to provide quantitative characteristics of the foam macroscopic morphologies (**Table 2**).

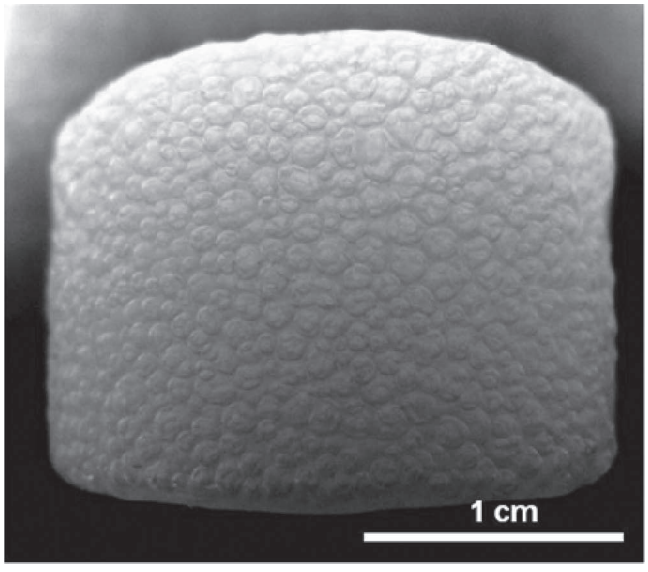

Figure6. Example of the final solid foam, $_{1.1}$Si(PHIPE)$_{64P}$ bearing millimeter-sized macropores.

Table 1. Mercury intrusion porosimetry data of the $_{X}$Si(PHIPE)$_{YZ}$ foams as a function of the oil type and amount of particles used to prepare the templating emulsions.

Solid state foam	Porosity [%]	Intrusion volume [cm^3 g^{-1}]	Bulk density [g cm^{-3}]	Skeletal density [g cm^{-3}]
$_{11.4}$Si(PHIPE)$_{64H}$	57	1.5	0.38	0.88
$_{4.8}$Si(PHIPE)$_{64H}$	60	1.5	0.40	1.00
$_{2.6}$Si(PHIPE)$_{64H}$	73	2.8	0.26	0.97
$_{7.3}$Si(PHIPE)$_{64P}$	73	3.1	0.23	0.86
$_{5.5}$Si(PHIPE)$_{64P}$	70	2.8	0.25	0.85
$_{3.7}$Si(PHIPE)$_{64P}$	75	3.0	0.25	1.03
$_{2.5}$Si(PHIPE)$_{64P}$	75	3.7	0.20	0.81
$_{1.1}$Si(PHIPE)$_{64P}$	71	3.2	0.22	0.77

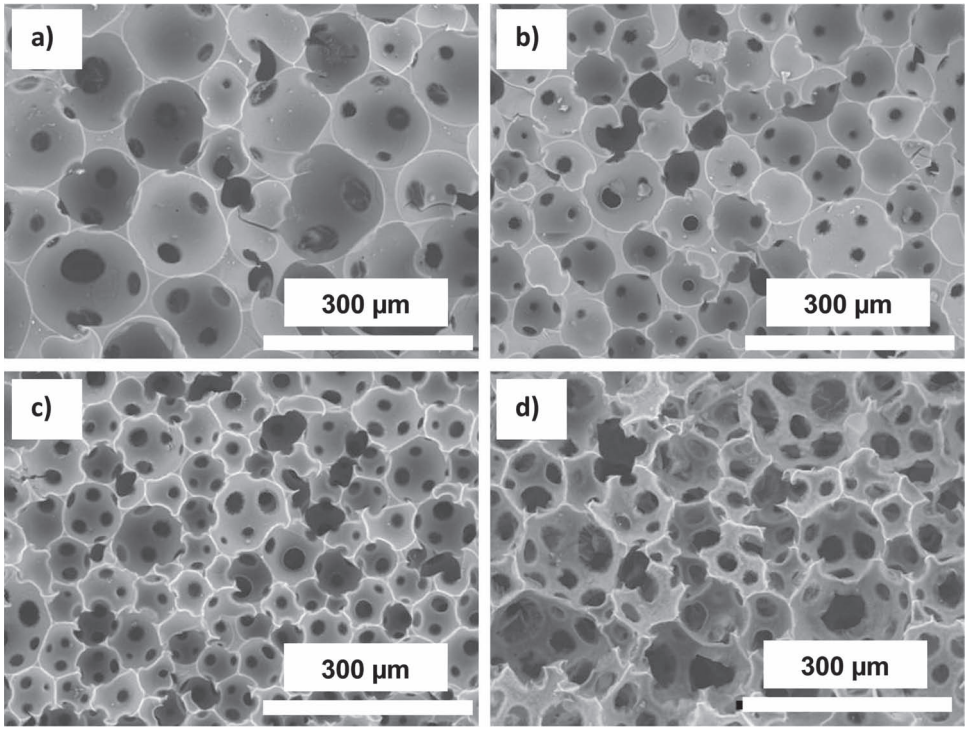

Figure 7. SEM images of sintered solid foams synthesized from hexadecane-in-water emulsions containing an increasing internal phase volume fraction: a) $_{2.6}$Si(PHIPE)$_{64H}$, b) $_{2.6}$Si(PHIPE)$_{75H}$, c) $_{2.6}$Si(PHIPE)$_{85H}$, and d) $_{2.3}$Si(PHIPE)$_{90H}$.

First, considering Table 2, we notice that the percentage porosity is increased as we increase the oil volume fraction, as confirmed by the increase of mercury intrusion volume. Also, from Table 1 and 2 we can notice that these foams skeletal density is around 1 g cm^{-3}, that is to say two times lower than the one for amorphous silica (2.3 g cm^{-3}) bearing intrinsic microporosity[63] (intrinsic microporosity is promoted through the statistical spatial repartition of the SiO_4 tetrahedra). Such a low density reveals that the foams are likely mesoporous, an interesting property that would even increase their surface areas. Such an issue will be discussed in the next section dedicated to the foams surface area, determined using nitrogen physisorption measurements.

Here, mercury porosimetry is particularly useful as it directly provides the evolution of the cell interconnecting windows and not the cells themselves (**Figure 8**). As the oil concentration increases (above 64 vol%), the droplets in close contact are compressed and locally deform, increasing the contact zones and forming flat films that gives rise to the connecting windows

Table 2. Mercury intrusion porosimetry data of the $_{X}$Si(PHIPE)$_{YH}$ foams as a function of the initial oil volume fraction of the templating emulsions.

Solid - state foam	Porosity [%]	Intrusion volume [cm^3 g^{-1}]	Bulk density [g cm^{-3}]	Skeletal density [g cm^{-3}]
$_{2.6}$Si(PHIPE)$_{64H}$	73	2.8	0.26	0.97
$_{2.6}$Si(PHIPE)$_{70H}$	74	2.8	0.26	1.02
$_{2.6}$Si(PHIPE)$_{75H}$	80	4.2	0.19	0.98
$_{2.6}$Si(PHIPE)$_{80H}$	78	3.4	0.23	1.05
$_{2.6}$Si(PHIPE)$_{85H}$	83	4.7	0.17	1.02
$_{2.3}$Si(PHIPE)$_{90H}$	92	11	0.08	1.10

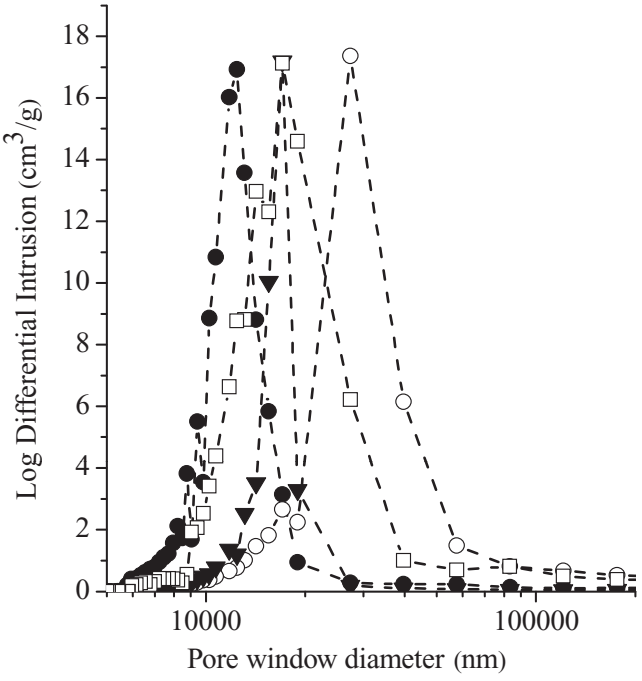

Figure 8. Examples of pore size distribution obtained from mercury porosimetry: (plain circles) $_{2.6}$Si(PHIPE)$_{64H}$; (squares) $_{2.6}$Si(PHIPE)$_{80H}$, (triangles) $_{2.6}$Si(PHIPE)$_{85H}$, and (empty circles) $_{2.3}$Si(PHIPE)$_{90H}$.

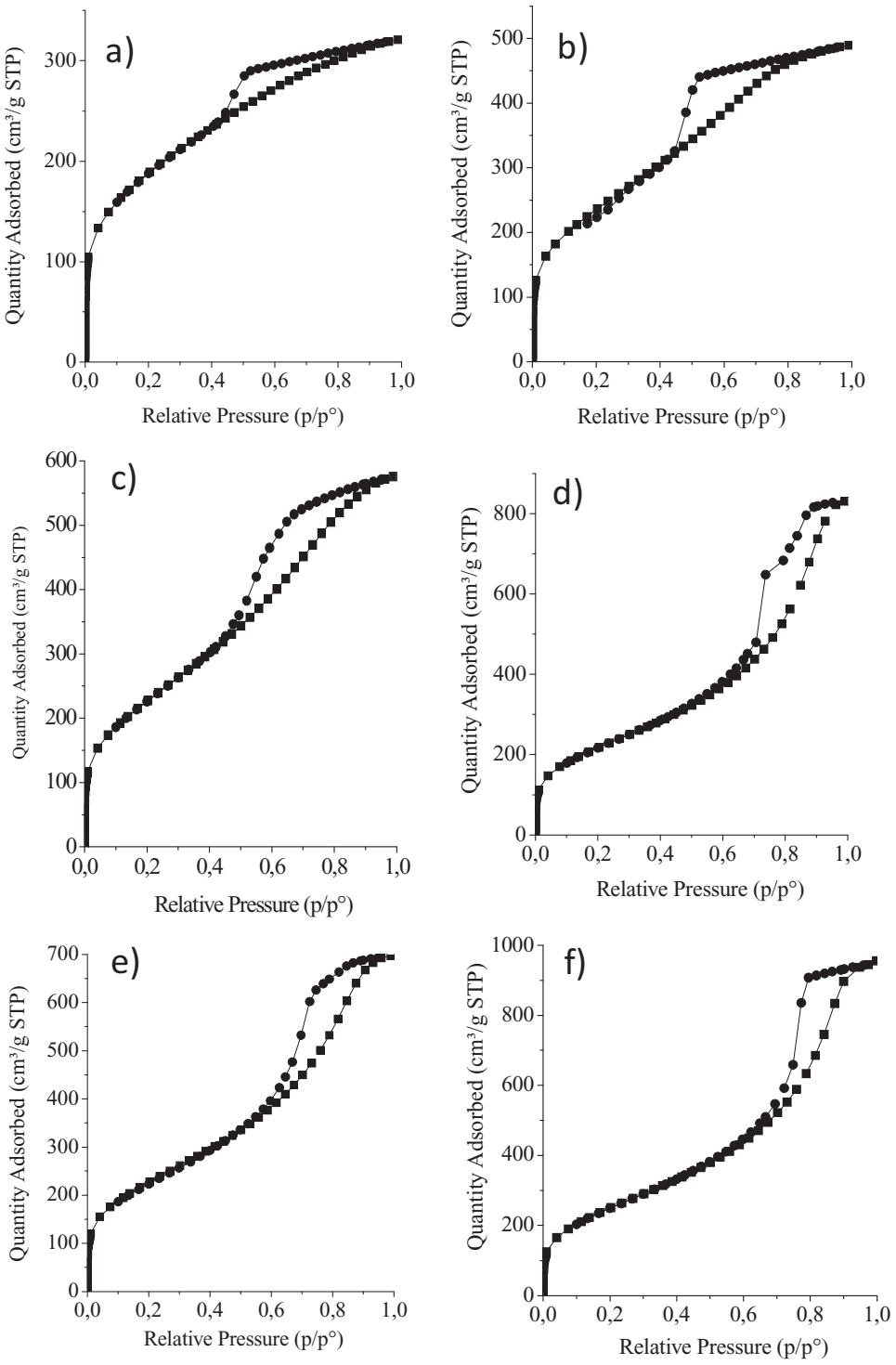

Figure 9. Nitrogen physisorption measurements for some $_{X}$Si(PHIPE)$_{YZ}$ foams: a) $_{4.8}$Si(PHIPE)$_{64H}$, b) $_{2.6}$Si(PHIPE)$_{64H}$, c) $_{2.6}$Si(PHIPE)$_{85H}$, d) $_{7.3}$Si(PHIPE)$_{64P}$, e) $_{3.7}$Si(PHIPE)$_{64P}$, and f) $_{1.1}$Si(PHIPE)$_{64P}$. Squares represent the adsorption curves; circles correspond to the desorption curves.

after mineralization and drying steps. The larger the initial contact zones, the larger the final connecting windows. As a consequence, considering Figure 8, it is possible to tune the diameter of connecting windows from 10 to 35 μm, in agreement with the SEM images in Figure 7.

At that point, it is of importance to characterize the solidified walls porosity. First, when considering the emulsification process, a very low amount of cationic CTAB surfactant is used to electrostatically adsorb at the negatively charged silica surface, as described elsewhere. Therefore, we should not

Table 3. Nitrogen physisorption data of the $_{X}$Si(PHIPE)$_{YZ}$ foams.

Solid - state foam	BET surface area [$m^2\ g^{-1}$]	Total pore volume [$cm^3\ g^{-1}$]	BJH[a)] surface area [$m^2\ g^{-1}$]	Average pore diameter [nm ± 1 nm]
$_{11.4}$Si(PHIPE)$_{64H}$	734	0.80	429	
$_{4.8}$Si(PHIPE)$_{64H}$	661	0.49	233	4
$_{2.6}$Si(PHIPE)$_{64H}$	844	0.76	447	4
$_{2.6}$Si(PHIPE)$_{70H}$	731	0.80	428	4
$_{2.6}$Si(PHIPE)$_{75H}$	767	0.79	502	4
$_{2.6}$Si(PHIPE)$_{80H}$	772	0.70	402	5
$_{2.6}$Si(PHIPE)$_{85H}$	823	0.89	526	5
$_{2.3}$Si(PHIPE)$_{90H}$	885	1.04	586	5
$_{7.3}$Si(PHIPE)$_{64P}$	780	1.28	566	8
$_{5.5}$Si(PHIPE)$_{64P}$	778	1.12	544	8
$_{3.7}$Si(PHIPE)$_{64P}$	815	1.08	547	8
$_{2.5}$Si(PHIPE)$_{64P}$	806	1.14	561	9
$_{1.1}$Si(PHIPE)$_{64P}$	917	1.48	699	11

[a)]BJH calculation valid for pore sizes between 1.7 and 50 nm, calculated from the adsorption curves.

generate mesoporosity emerging from templating lyotropic mesophases. Representative nitrogen physisorption data are depicted in **Figure 9**: the adsorption/desorption curves are characteristics of type I–IV isotherms[64] associated with materials bearing both micro- and mesoporosity.

Microporosity is expected as it emerges from the inherent SiO_4 tetrahedra random repartition in space, silica being an amorphous material in the present synthetic route. This microporosity is responsible for the high slope adsorption curve observed at low relative $P/P°$ values (Figure 9). The micropore volume read from the isotherms is almost constant, around 0.2 $cm^3\ g^{-1}$ for all materials, which is consistent with the intrinsic nature of microporosity. At $P/P°$ values above 0.5, the nitrogen physisorption measurements present a hysteresis between the adsorption and desorption curves. This is characteristic of type IV isotherms and demonstrates without ambiguity the mesoporous character of those Si(PHIPE) foams. Indeed, considering the values proposed within **Table 3**, these foams bear Brunauer, Emmet and Teller (BET) surface area ranging from 700 to 900 $m^2\ g^{-1}$ while the mesoporosity (Barett, Joyner, Halenda (BJH) calculations) ranges from 200 to 700 $m^2\ g^{-1}$.

Beyond mesoporosity evaluation, by using the desorption curves, the BJH pore sizes distribution can be estimated (**Figure 10**). The first main feature is that mesoporosity is around 4 nm for $_{X}$Si(PHIPE)$_{YH}$ foams and 8 nm for $_{X}$Si(PHIPE)$_{YP}$ materials, which reflects their difference in contraction factor. The second main characteristic is that the mesoscopic pore size distributions are rather monodisperse in all cases. Again, these values of pore size cannot be explained with lyotropic mesophases acting as templating agent, as the CTAB concentration is by far too low (far below the CMC). For instance, when compared with a former study where Si(HIPE) materials were obtained using CTAB molecules as templates, the mesopores sizes distribution were rather polydisperse (vermicular type), with pore diameters being smaller or equal to 2 nm.[17] The sol–gel process occurs here at pH close to zero ($[H_3O^+] \approx 4$–6 M), that is to say much below the silica isoelectric point obtained at pH 2.1, and without surfactant in the continuous phase. Considering such low pH, the silica condensation will provide a dual Fractal–Euclidian character to the on-growing inorganic polymer.[63] This dual character can explain on one hand the microporosity, associated to the fractal character and, on the other hand, the mesoporosity due to interstices between nanoclusters associated to the Euclidian character. Since the sol–gel pH conditions are essentially the same for all the samples proposed here, the final mesoporosity should vary only through the type of oil that modifies the volume contraction rate. To assess this explanation, we performed TEM investigations to visualize the nature of the mesoporosity evidenced through the nitrogen physisorption measurements. As observed in **Figure 11**, whatever the $_{X}$Si(PHIPE)$_{YZ}$ series, the foam walls are made of silica nanoclusters tighly packed together, the clusters themselves bearing the microporosity responsible for the nitrogen adsorption at low $P/P°$ (Figure 9). We can observe that the nanoclusters are randomly dispersed (in space), and the mesoporosity emerges from the nanoclusters packing interstices. For a given foam, the nanoclusters are rather homogeneous in size without any specific shape. We notice in Figure 11 that, due to limited TEM resolution,we are not able to differentiate the $_{X}$Si(PHIPE)$_{YH}$ 4–6 nm mesoporosity from the 8–12 nm mesopores of the $_{X}$Si(PHIPE)$_{YP}$.

The homogeneity in size of the mesopores can result from the particles growth governed by dissolution-precipitation, namely Ostwald ripening.[63] Also, as the particles do not possess any specific shape, the inter-particles void space will be pore cavities larger in diameter than the openings (throats) – so-called ink-bottle pores.[63,64]

4. Conclusions

We have shown a new and easy route to produce macrocellular solid foams from Pickering emulsions. Exploiting the limited coalescence process occurring in these solid-stabilized

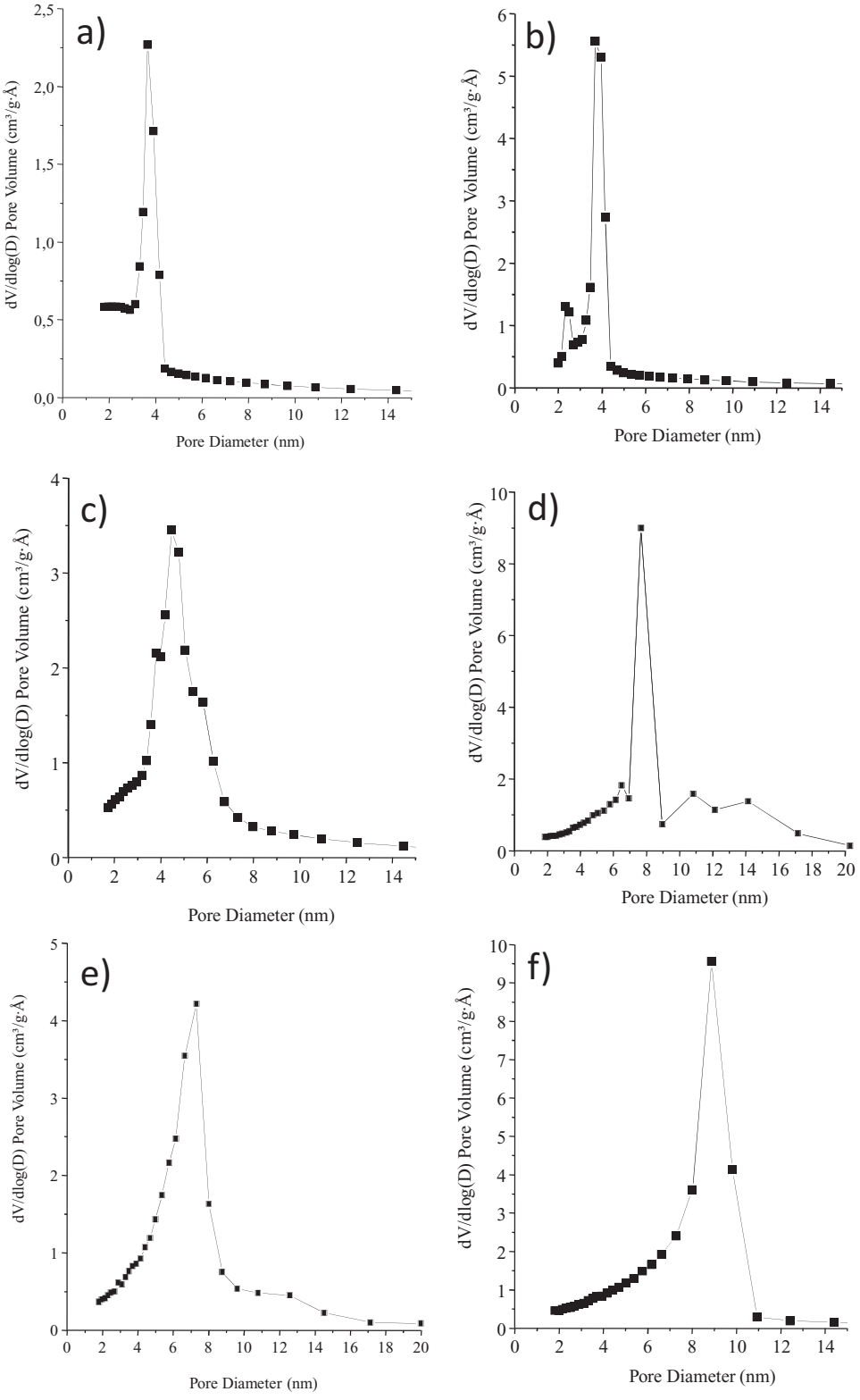

Figure 10. Pore sizes distribution for some $_{X}$Si(PHIPE)$_{YZ}$ foams: a) $_{4.8}$Si(PHIPE)$_{64H,}$ b) $_{2.6}$Si(PHIPE)$_{64H,}$ c) $_{2.6}$Si(PHIPE)$_{85H}$, d) $_{7.3}$Si(PHIPE)$_{64P,}$ e) $_{3.7}$Si(PHIPE)$_{64P,}$ and, f) $_{1.1}$Si(PHIPE)$_{64P.}$ Calculated from the BJH desorption curves.

emulsions, we get very well-controlled emulsion properties (drop size and dispersed phase volume fraction). Such a good control over the initial emulsions formulation and sol-gel process allows elaboration of porous monoliths with i) narrow macropore size distribution, ii) controlled macropore size ranging from the micrometer to the millimeter,

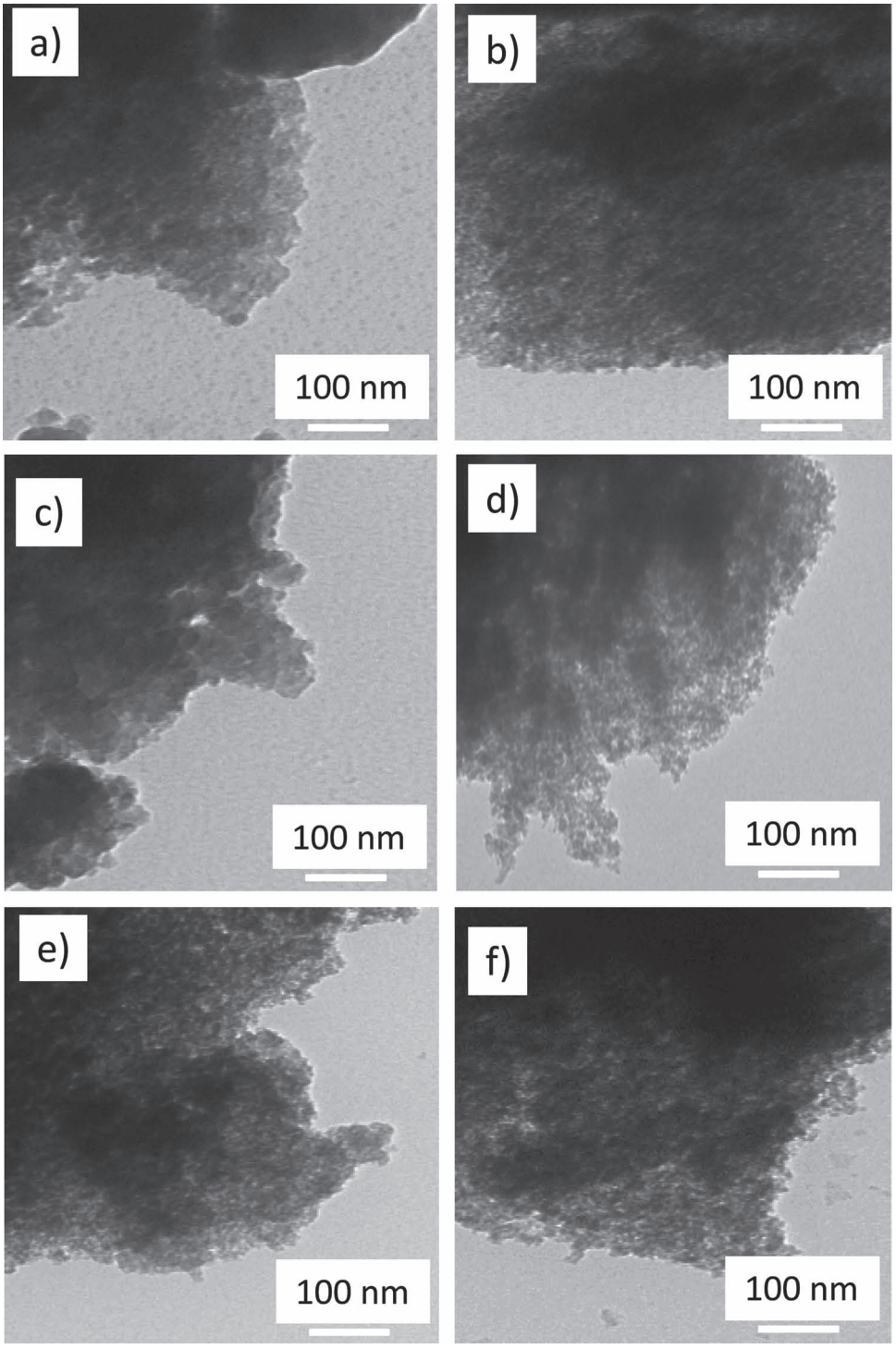

Figure 11. TEM observations for some characteristic foams: a) $_{4.8}$Si(PHIPE)$_{64H}$, b) $_{2.6}$Si(PHIPE)$_{64H}$, c) $_{2.6}$Si(PHIPE)$_{85H}$, d) $_{7.3}$Si(PHIPE)$_{64P}$, e) $_{3.7}$Si(PHIPE)$_{64P}$, and, f) $_{1.1}$Si(PHIPE)$_{64P}$.

iii) narrow window size, and iv) tunable macroporosity. These macrocellular foams exhibit both micro- and mesoporosity leading to BET values between 700 and 900 $m^2\ g^{-1}$ with a good monodispersity of the mesopores.

These novel macrocellular monoliths bearing both monodisperse and tunable macroporosity are outstanding candidates as models for acoustic and thermal insulator investigations. They can also provide very high insights into diverse selective membrane applications. Moreover, when used as hard templates such as basic Si(HIPE) materials, they may promote calibrated macroporous carbonaceous electrodes,[65] thereby advancing model electrodes for biofuel cell[66,67] applications.

Supporting Information

Supporting Information is available from the Wiley Online Library or from the author.

Acknowledgements

The authors thank Dr. Jean-Paul Salvetat for acquiring the TEM pictures.

Received: October 24, 2011
Revised: December 28, 2011
Published online: March 29, 2012

[1] N. R. Cameron, P. Krajnc, M. S. Silverstein, in *Porous Polymer*, (Eds: M. S. Silverstein, N.R. Cameron, M. A. Hillmyer) John Wiley & Sons, Inc., Hoboken, NJ **2011**, *119*, Ch. 2.
[2] N. Brun, S. Ungureanu, H. Deleuze, R. Backov, *Chem. Soc. Rev.* **2011**, *40*, 771.
[3] C.-M. Chung, T. P. Chou, G. Cao, J.-G. Kim, *Mater. Chem. Phys.* **2006**, *95*, 260.
[4] D. C. Sherrington, in:*Polymer Supported Reactions in Polymer Supported reactions in Organic Synthesis*, (Eds D. C. Sherrington, P. Hodge), Wiley, Chichester, UK **1980**.
[5] P. Hodge, in: *Synthesis and Separations using Functional Polymers*, (Eds: D. C. Sherrington, P. Hodge), Wiley, Chichester, UK **1998**.
[6] H. Zhang, A. I. Cooper, *Soft Matter* **2005**, *1*, 107.
[7] R. Backov, *Soft Matter* **2006**, *2*, 452.
[8] E. Prouzet, S. Ravaine, C. Sanchez, R. Backov, *New J. Chem.* **2008**, *32*, 1284.
[9] E. Prouzet, Z. Khani, M. Bertrand, M. Tokumoto, V. Gyuot-Ferreol, J.-F. Tranchant, *Microporous Mesoporous Mater.* **2006**, *96*, 369.
[10] G. A. Ozin, *Chem. Commun.* **2000**, *6*, 419.
[11] C. Sanchez, H. Arribart, M. Giraud-Guille, *Nat. Mater.* **2005**, *4*, 277.
[12] A.-W. Xu, Y. Ma, H. Cölfen, *J. Mater. Chem.* **2007**, *17*, 415.
[13] C. Sanchez, J. Ribot, *New J. Chem.* **1994**, *18*, 1007.
[14] C. Sanchez, B. Julian, P. Belleville, M. Popall, *J. Mater Chem.* **2005**, *15*, 3559.
[15] P. Gómez-Romero, C. Sanchez, *Functional Hybrid Materials*, (Eds: P. Gómez-Romero, C. Sanchez), Wiley-VCH, Weinheim, Germany **2003**.
[16] A. Imhof, D. J. Pine, *Adv. Mater.* **1998**, *10*, 697.
[17] F. Carn, A. Colin, M.-F. Achard, H. Deleuze, M. Birot, R. Backov, *J. Mater. Chem.* **2004**, *14*, 1370.
[18] G. T. Chandrappa, N. Steunou, J. Livage, *Nature* **2002**, *416*, 702.
[19] H. Maekawa, J. Esquena, S. Bishop, C. Solans, B. F. Chmelka, *Adv. Mater.* **2003**, *15*, 591.
[20] D. Walsh, A. Kulak, K. Aoki, T. Ikoma, J. Tanaka, S. Mann, *Angew. Chem., Int. Ed.* **2004**, *43*, 6691.
[21] F. Carn, N. Steunou, A. Colin, J. Livage, R. Backov, *Chem. Mater.* **2005**, *17*, 644.
[22] F. Carn, P. Masse, H. Saadaoui, B. Julián-López, H. Deleuze, S. Ravaine, C. Sanchez, D. R. Talham, R. Backov, *Langmuir* **2006**, *22*, 5469.
[23] F. Carn, M.-F. Achard, O. Babot, H. Deleuze, S. Reculusa, R. Backov, *J. Mater. Chem.* **2005**, *15*, 3887.
[24] F. Carn, A. Derré, W. Neri, O. Babot, H. Deleuze, R. Backov, *New J. Chem.* **2005**, *29*, 1346.
[25] C. M. Leroy, F. Carn, M. Trinquecost, R. Backov, P. Delhaès, *Carbon* **2007**, *45*, 2317.
[26] B. T. Holland, C.F. Blanford, A. Stein, *Science* **1998**, *281*, 538.
[27] M. Antonietti, B. Berton, C. Göltner, H.-P. Hentze, *Adv. Mater.* **1998**, *10*, 154.
[28] S. Busch, H. Dolhaine, A. DuChesne, S. Heinz, O. Hochrein, F. Laeri, O. Podebrad, U. Vietze, T. Weiland, R. Kniep, *Eur. J. Inorg. Chem.* **1999**, *10*, 1643.
[29] C. M. Leroy, M.-F. Achard, O. Babot, N. Steunou, P. Masse, J. Livage, L. Binet, N. Brun, R. Backov, *Chem. Mater.* **2007**, *19*, 3988.
[30] I. S. Chronakis, *J. Mater. Process. Tech.* **2005**, *167*, 283.
[31] A. Imhof, D. J. Pine, *Nature* **1997**, *389*, 948.
[32] G.-R. Yi, S. M. Yang, *Chem. Mater.* **1999**, *11*, 2322.
[33] D. Barby, Z. Haq, *Eur. Pat. 0060138* **1982**.
[34] N. R. Cameron, D. C. Sherrington, *Adv. Polym. Sci.* **1996**, *126*, 163.
[35] N. R. Cameron, *Polymer* **2005**, *46*, 1439.
[36] H. Tai, A. Sergienko, M. S. Silverstein, *Polymer* **2001**, *42*, 4473.
[37] S. Ungureanu, M. Birot, L. Guillaumme, H. Deleuze, O. Babot, M.-F. Achard, M. I. Popa, C. Sanchez, R. Backov, *Colloids Surf., A* **2010**, *360*, 85
[38] H. Zhang, G. C. Hardy, M. J. Rosseinsky, A. I. Cooper, *Adv Mater.* **2003**, *15*, 78.
[39] S. Ungureanu, M. Birot, G. Laurent, H. Deleuze, O. Babot, B. Julian-Lopez, M.-F. Achard, M. I. Popa, C. Sanchez, R. Backov, *Chem. Mater.* **2007**, *19*, 5786.
[40] H. Zhang, G. C. Hardy, Y. Z. Khimyak, M. J. Rosseinsky, A. I. Cooper, *Chem. Mater.* **2004**, *16*, 4245.
[41] M. S. Silverstein, H.W Tai, A. Sergienko, Y. L. Lumelsky, S. Pavlovsky, *Polymer* **2005**, *46*, 6682.
[42] H. Zhang, A. I. Cooper, *Ind. Eng. Chem. Res.* **2005**, *44*, 8707.
[43] N. Brun, A. Babeau-Garcia, H. Deleuze, F. Duran, C. Sanchez, V. Ostreicher, R. Backov, *Chem. Mater.* **2010**, *22*, 4555.
[44] J. Normatov, M. S. Silverstein, *Polymer* **2007**, *48*, 6648.
[45] S. Ungureanu, M. Birot, H. Deleuze, O. Babot, M.-F. Achard, M. I. Popa, C. Sanchez, R. Backov, *Appl. Catal., A* **2010**, *390*, 51.
[46] J. Normatov, M. S. Silverstein, *Macromolecules* **2007**, *40*, 8329.
[47] N. Brun, A. Babeau-Garcia, M.-F. Achard, C. Sanchez, F. Durand, L. Guillaume, M. Birot, H. Deleuze, R. Backov, *Energy Environ. Sci.* **2011**, *4*, 2840.
[48] J. Normatov, M. S. Silverstein, *Chem. Mater.* **2008**, *20*, 1571.
[49] J. Normatov, M. S. Silverstein, *J. Polym. Sci., Part A: Polym. Chem.* **2008**, *46*, 2357.
[50] S. U. Pickering, *J. Chem. Soc.* **1907**, *91*, 2001.
[51] B. P. Binks, *Curr. Opin. Colloid Interface Sci.* **2003**, *7*, 21.
[52] F. Leal-Calderon, V. Schmitt, *Curr. Opin. Colloid Interface Sci.* **2007**, *13*, 217
[53] P. J. Colver, A. F. Bon, *Chem. Mater.* **2007**, *19*, 1537.
[54] V. O. A. Ikem, A. Menner, A. Bismarck, *Angew. Chem., Int. Ed.* **2008**, *47*, 8277.
[55] M. C. Hermant, B. Klumperman, C. E. Koning, *Chem. Commun.* **2009**, 2738.
[56] A. Menner, R. Verdejo, M. Shaffer, A. Bismarck, *Langmuir* **2007**, *23*, 2398.
[57] I. Akartuna, A. R. Studart, E. Tervoort, L. Gauckler, *Adv. Mater.* **2008**, *20*, 4714.
[58] B. P. Binks, *Adv. Mater.* **2002**, *14*, 1824.
[59] I. Aranberry, B. P. Binks, J. H. Clint, P. D. I. Fletcher, *J. Porous Mater.* **2009**, *16*, 429.
[60] S. Arditty, C. Whitby, V. Schmitt, B. P. Binks, F. Leal-Calderon, *Eur. Phys. J. E* **2003**, *11*, 273.
[61] J. Giermanska-Kahn, V. Laine, S. Arditty, V. Schmitt, F Leal-Calderon, *Langmuir* **2005**, *21*, 4316.
[62] M. Destribats, V. Schmitt, R. Backov, *Langmuir* **2010**, *26*, 1734.

[63] C. J. Brinker, G. W. Scherer, *Sol-Gel Science: the Physics and Chemistry of Sol-Gel Processing*, Academic Press, San Diego **1990**.
[64] P. A. Webbs, C. Orr, *Analytical Methods in Fine Particle Technology*, Micromeritics Instrumentations Corporation, NorcrossGA **1997**, Ch. 3.
[65] a) N. Brun, S. R. S. Prabahan, M. Birot, C. Sanchez, M. Morcrette, G. Pécastaing, A. Soum, H. Deleuze, R. Backov, *Adv. Funct. Mater.* **2009**, *19*, 3136; b) N. Brun, S. R. S. Prabaharan, M. Morcrette, H. Deleuze, M. Birot, O. Babot, M.-F. Achard, C. Surcin, R. Backov, *J. Chem. Phys. C* **2012**, *116*, 1408.
[66] V. Flexer, N. Brun, R. Backov, N. Mano, *Energy Environ. Sci.* **2010**, *3*, 1302.
[67] V. Flexer, N. Brun, O. Courgean, R. Backov, N. Mano, *Energy Environ. Sci.* **2011**, *4*, 2097.